Solar Wind Associated with Near Equatorial Coronal Hole

M. Hegde[1,2,*], K. M. Hiremath[1], Vijayakumar H. Doddamani[2]
& Shashanka R Gurumath[3]

[1]*Indian Institute of Astrophysics, Bengaluru 560 034, India.*
[2]*Department of Physics, Bangalore University, Bengaluru 560 056, India.*
[3]*School of Advanced Studies, VIT University, Vellore 632 014, India.*
[*]*e-mail: manjunath@iiap.res.in*

Abstract. Present study probes temporal changes in the area and radiative flux of near equatorial coronal hole associated with solar wind parameters such as wind speed, density, magnetic field and temperature. Using high temporal resolution data from SDO/AIA for the two wavelengths 193 Å and 211 Å, area and radiative flux of coronal holes are extracted and are examined for the association with high speed solar wind parameters. We find a strong association between different parameters of coronal hole and solar wind. For both the wavelength bands, we also compute coronal hole radiative energy near the earth and it is found to be of similar order as that of solar wind energy. However, for the wavelength 193 Å, owing to almost similar magnitudes of energy emitted by coronal hole and energy due to solar wind, it is conjectured that solar wind might have originated around the same height where 193 Å line is formed in the corona.

Key words. Sun: coronal hole—Sun: solar wind.

1. Introduction

Coronal Holes (CH) are large regions ($\sim 10^{20}$ cm^2) in solar corona having open magnetic field structure (Altschuler *et al.* 1972; Hiremath & Hegde 2013). Due to their lower coronal temperature ($\sim 10^6$ K) compared to ambient temperature and low density, CHs have reduced emission at X-ray and extreme ultraviolet wavelengths, and hence can be identified as dark regions (Krista 2012 and references therein) in these wavelength images. Madjarska & Wiegelmann (2009) classified CHs mainly into two categories depending on the position in solar coronal images viz. polar coronal holes and equatorial coronal holes respectively.

Solar wind is a continuous stream of electrons, protons and ionized particles emanating from the sun. Solar wind plays a vital role in shaping the heliosphere and substantially interacts in the near-Earth environment. Probably, during the early history of solar system formation, strong solar wind might have played a dominant role

in blowing of tenuous atmospheres of some of the low mass terrestrial planets (Wood 2006; Shashanka *et al.* 2014a, b).

According to Marsch (1999), solar wind can be generally classified into three types: the steady fast wind (>600 km/s) originating from the open magnetic field regions in coronal holes (Krieger *et al.* 1973; Zirker 1977), the unsteady slow wind (∼400 km/s) that emanate from the temporarily open streamer belt, and the transient wind caused by large coronal mass ejections. Following Axford & McKenzie (1997), Xia (2003) summarized two basic types (fast and slow) of solar wind with average physical properties at 1 AU that are presented in Table 1.

Biermann (1951), from the study of cometary tails pointed out that continuous particles are streaming out from the Sun. Parker (1958) predicted that the outer-most atmosphere of the Sun viz., the corona can not remain in static equilibrium but must be continually evolving its structure and dynamics leading to the gene-sis of slow solar wind. A close association between the speed of the high speed solar wind streams and coronal hole area that have a positive correlation is reported by Nolte *et al.* (1976). Several studies (Sheeley & Harvey 1981; Wang & Sheeley 1990; Gosling & Pizzo 1999; Zhang *et al.* 2002, 2003; McComas *et al.* 2002; Bromage *et al.* 2001; Robbins *et al.* 2006; Vršnak *et al.* 2007a, b; Abramenko *et al.* 2009; Verbanac *et al.* 2011) have investigated the statistical relationship between coronal holes and studied how their changes in size and location control the solar wind parameters and simultaneously affect geomagnetic field structure. Vršnak *et al.* (2007a, b) considered fractional area of coronal hole near the central meridian for their analysis and used daily averaged area of CHs near the disk centre and the daily average solar wind properties during the solar minimum.

Using 9 years of data from the YOHKOH/SXT, Kahler & Hudson (2001) deter-mined the properties of 19 transient coronal holes (mid- and low-latitude) and showed several interesting characteristics viz., they are generally small in size, occur in

Table 1. Two modes of solar wind flow (Axford & McKenzie 1997). Extracted from Xia (2003).

Property (1 AU)	Low speed	High speed
Speed (V)	<400 km s^{-1}	700–900 km s^{-1}
Density (n)	∼10 cm^{-3}	∼3 cm^{-3}
Flux (nV)	∼3 × 10^8 cm^{-2} s^{-1}	∼2 × 10^8 cm^{-2} s^{-1}
Magnetic field (B_r)	∼2.8 nT	∼2.8 nT
Temperatures	$T_p \sim 4 \times 10^4$ K	$T_p \sim 2 \times 10^5$ K
	$T_e \sim 1.3 \times 10^5$ K	$T_e \sim 10^5$ K
Coulomb collisions	Important	Negligible
Anisotropy	T_p isotropic	$T_p (\perp) > T_p (\parallel)$
Beams	None	Fast ion beams + electron strahl
Structure	Filamentary, highly variable	Uniform, slow change
Composition	He/H ∼1–30%	He/H ∼1–5%
Waves	Both directions	Outwards propagating
Associated with	Streamers, transiently open field	Coronal holes
Sunspot minimum	±15° from equator	>30°
Sunspot maximum	Dominant at most latitudes	Less frequent

T_p is proton temperature; T_e is electron temperature.

magnetic unipolar regions, trailing large active regions, typically have short lifetimes and are located in areas where the magnetic neutral line shows a large scale curvature. Janardhan *et al.* (Janardhan *et al.* 2008a, b) and Sakao *et al.* (2007 and references therein) studied mid-latitude coronal holes that lie alongside large active regions and found that combination of both led to highly non-radial solar wind flows that have extended Alfven radii. Verbanac *et al.* (2011), using 6 hours cadence data (four images per day), examined the association between CH characteristics (fractional area of CH), high speed solar streams (HSSs) parameters, and the geomagnetic activity indices. Shugai *et al.* (2009) examined association between
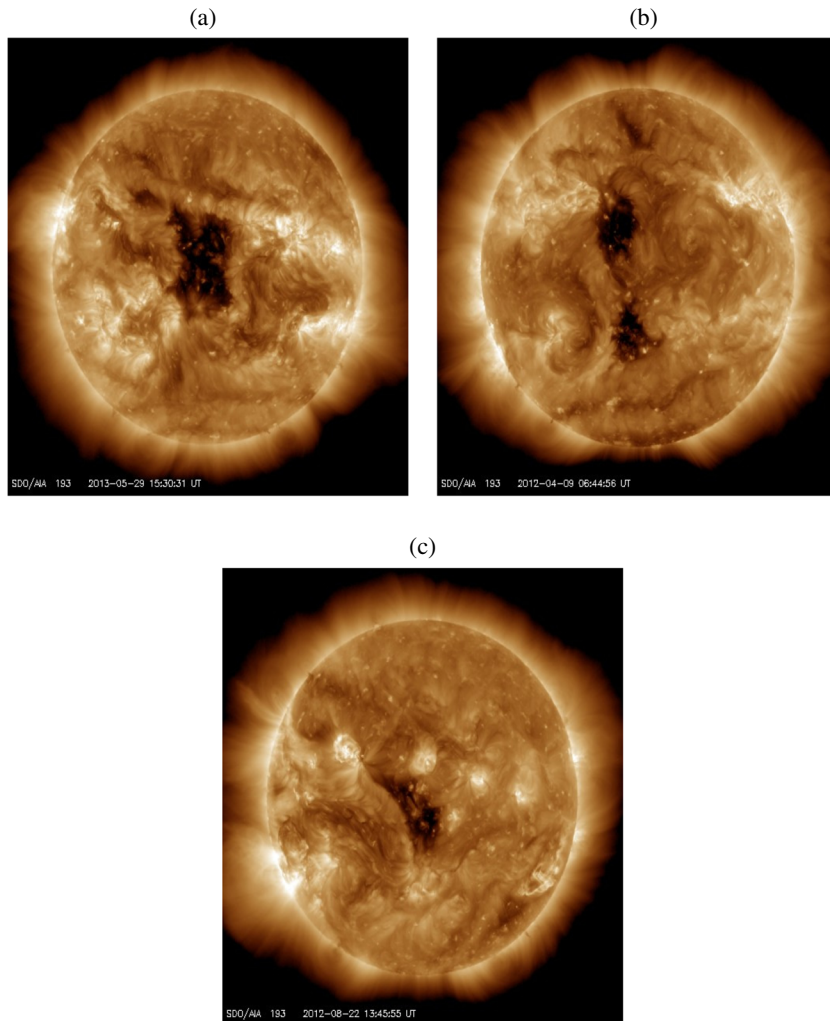
(a) (b)

(c)

Figure 1 (a), (b) and (c). Full-disk image of the sun observed in 211 Å band of SDO/AIA on 29-05-2013, 09-04-20012 and 22-08-2012 respectively are shown. The CH in the centre (equator) of the figure in all the three images indicates the region of interest for our study. Image credit: SDO/AIA.

geomagnetic activity, solar wind velocity and coronal hole area, and found a moderate correlation (0.40–0.65) with the coronal hole areas. Subramanian *et al.* (2010) studied the association between the coronal hole boundary and slow solar wind by using Hinode/XRT data and suggested plasma outflows triggered by magnetic reconnection that are possibly one of the sources of the slow solar wind. Comparison of the contrast of coronal holes (CH) with the solar wind parameters is studied by Obridko *et al.* (2009) and Obridko & Shelting (2011). In that study taking different travel times like 2, 3 and 4 days, correlation analysis was done using 284 Å wavelength.
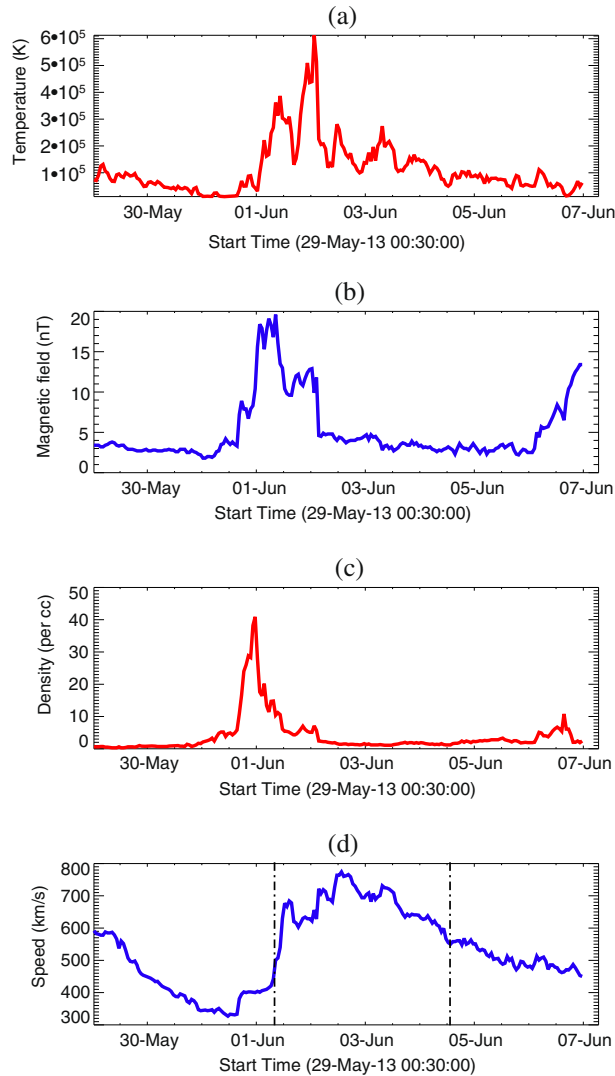

Figure 2(a)–(d). The variation of different parameters viz., proton temperature, magnitude of magnetic field, density and speed of solar wind (CH event 29-05-2013) respectively are shown. In Figure 2(d), dashed vertical lines indicate starting and end time of high speed wind.

To detect boundary of CH and to estimate areas, these studies used two different thresholds. Moreover, these studies did not take into account correction for the projection effect of area of CH. Considering extended minimum between cycles 23 and 24 CH data, de Toma (2011) examined the implications of the solar wind speed near the Earth and also compared the results for the minimum year 1996. Rotter *et al.* (2012) found that coronal hole area, position and intensity levels have positive correlation with the solar wind velocity at 1 AU. Akiyama *et al.* (2013) determined a strong positive correlation between the maximum solar speed and the area of EUV CH, and also between the maximum solar wind speed and the area of the microwave enhancement. Tlatov *et al.* (2014) reported that high latitude CHs affect the properties of the solar wind in the ecliptic plane.
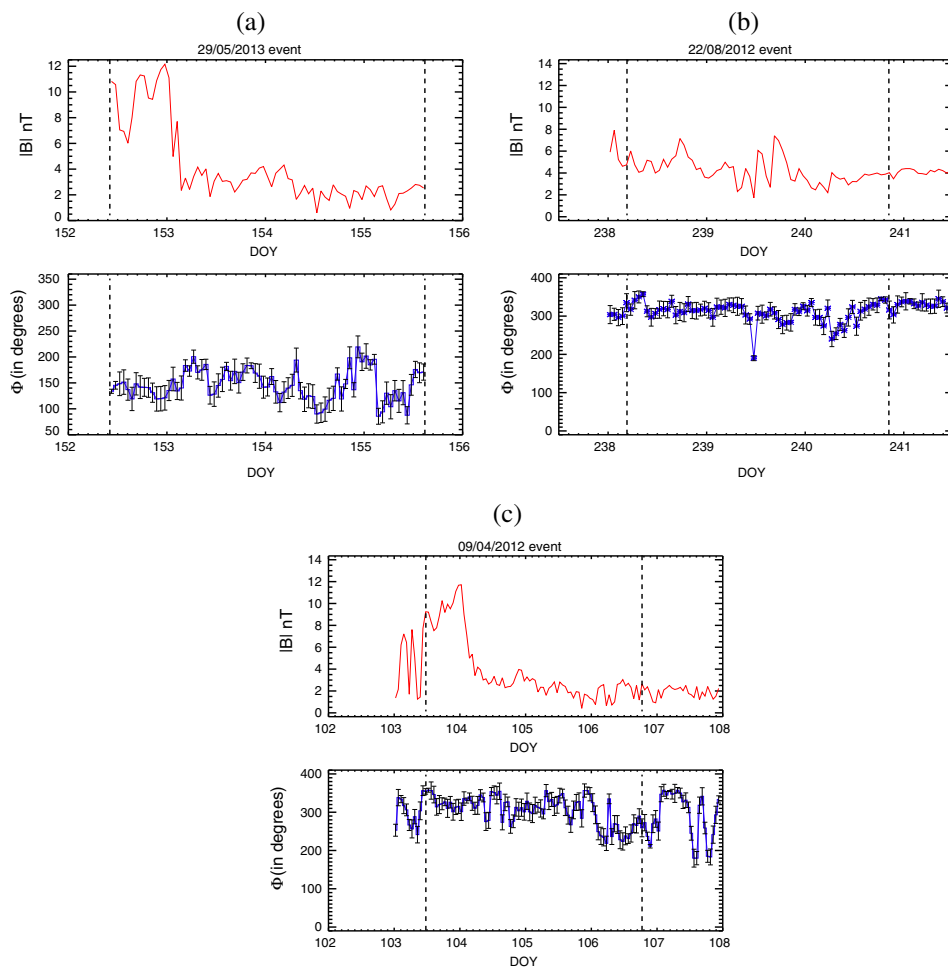

Figure 3. Magnitude of the magnetic field (upper panel) and azimuthal direction (lower panel) of the magnetic field in the ecliptic plane for the three solar wind events: **(a)** 29-05-2013 event, **(b)** 22-08-2012 event, **(c)** 09-04-2012 event. Event date has been demarcated in all the figures using dashed vertical lines.

Few of the aforementioned studies did not take into account correction for the projectional effect for area of CH and also the time cadence considered for those studies was comparatively large (∼6 h). Although CH contrast (Obridko *et al.* 2009) is considered for comparing with solar wind parameters, none of the studies calculated radiative flux emitted by CH and compared with the wind parameters.

Keeping all these views in mind, we applied projection correction for the area of CH and also computed radiative flux of the CH in order to compare whether energy of CH calculated from radiative flux is almost same as kinetic energy of the solar wind. Hence, this result ensures that fast solar wind on that day is solely due to the coronal hole that appeared on the solar disk. In order to achieve these goals, using the unprecedented continuous observations by SDO (Solar Dynamics Observatory)/AIA (Atmospheric Imaging Assembly), we have considered near equatorial coronal hole data with 1 hour time cadence.

Other aims of this study are: (i) like area of CH, do temporal variation of radiative flux that is originated from the coronal hole has any association with the solar wind parameters? (ii) whether computed radiative energy from CH at 1 AU matches with thermal or kinetic energy of the solar wind? (iii) at what height in the solar corona, solar wind probably is originated? With these aims in mind, we present the data used and method of analysis in section 2, and the results are presented in section 3. A brief discussion followed by conclusions are presented in section 4.

2. Data and analysis

Coronal hole data is considered from the AIA instrument (Lemen *et al.* 2012) on board the SDO. The instrument provides continuous data of full Sun with four
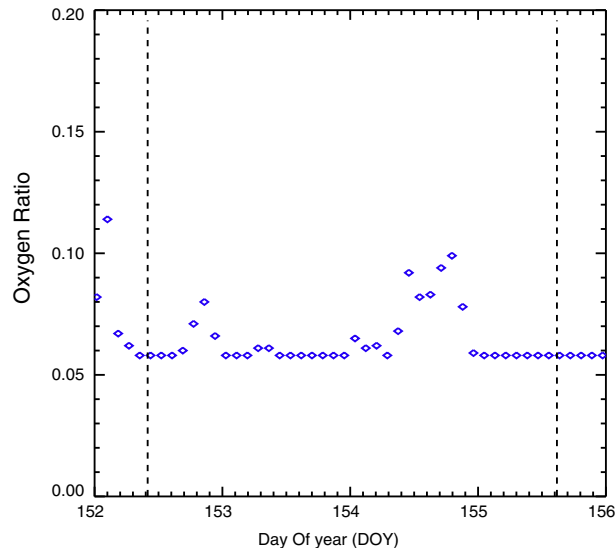

Figure 4. Variation of oxygen state ratio O^{7+}/O^{6+} for the event 29 May 2013 (DOY 152). Event date has been demarcated in the figure using dashed vertical lines.

4k × 4k detectors with a good spatial resolution. For our study, we considered equatorial CH image data from 193 Å (Fe XII, XXIV) and 211 Å (Fe XIV) passbands with 1 h cadence. Figure 1 illustrates the selected typical coronal hole images seen in 193 Å and 211 Å respectively. As time interval of observation is free from occurrence of coronal mass ejections, we can safely assume that fast solar wind more likely originated and is controlled by CH only. The solar wind data is considered from OMNI (http://cdaweb.gsfc.nasa.gov website) and different parameters of the solar wind considered for the analysis are: flow speed (km/s), magnitude of average magnetic field (nT), proton number density (/cc) and temperature (K) of the proton.

After calibrating the images of CH by aia_prep.pro and following the method of Hiremath & Hegde (2013) for two wavelength bands, coronal hole is detected and its average heliographic coordinates (longitude, l and latitude, θ) are computed. For each CH image, total number of pixels (TNP) and total data number (TDN) within
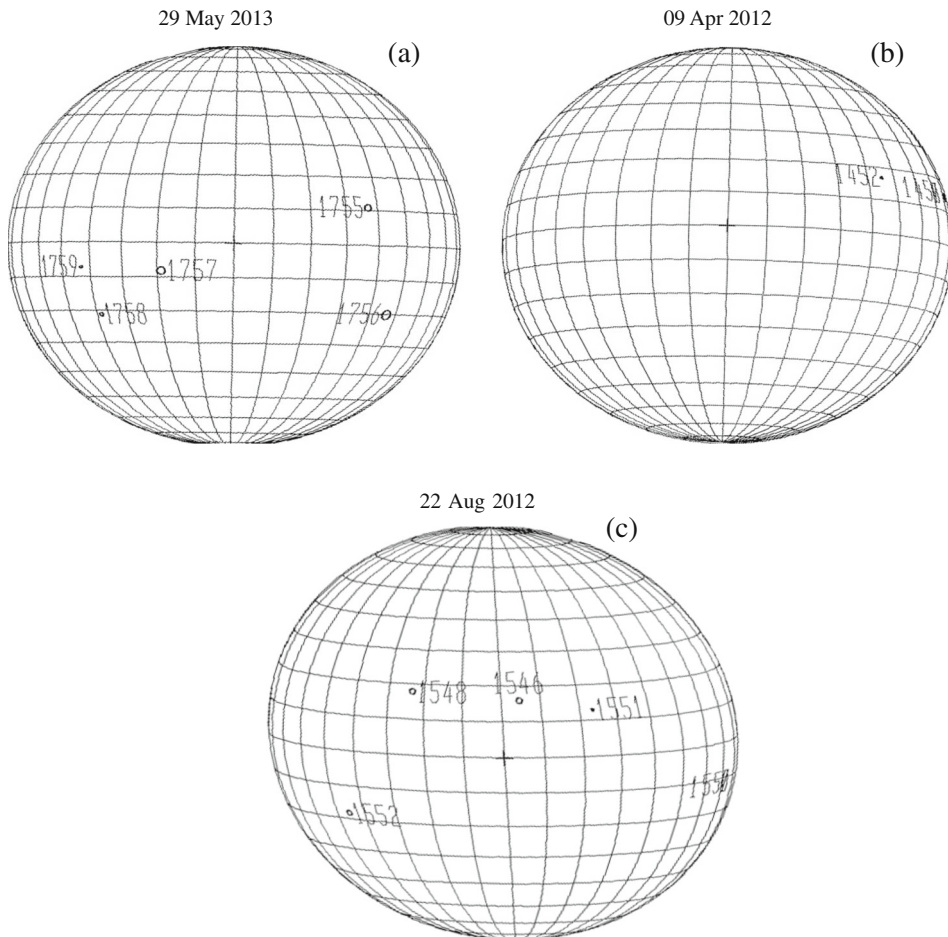

Figure 5. Active region maps obtained from the MEES obsevatory of the solar photosphere on **(a)** 29 May 2013 (DOY 149), **(b)** 09 April 2012 (DOY 100) and **(c)** 22 August 2012 (DOY 235) respectively, indicating the locations of the different active regions.
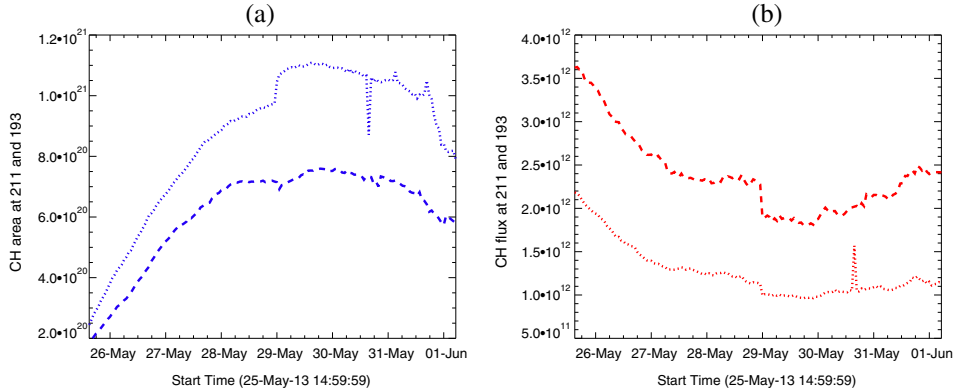
Figure 6. **(a)** Variation of area (cm^2) of the coronal hole in 193 Å (dashed line) and 211 Å (dotted line) pass bands are shown. **(b)** Variation of radiative flux (photons cm^{-2} s^{-1} sr^{-1}) of the coronal hole in 193 Å (dashed line) and 211 Å (dotted line) pass bands occurred on 29-05-2013 with respect to time.

the detected boundary region are estimated. By taking into account the projectional effect, area (A) of the coronal hole is computed as follows:

$$A = \frac{\text{TNP}}{\cos\ l} * 0.6 * 0.6 * 719 * 719 \ \text{cm}^2, \tag{1}$$

where l is the longitude from the central meridian. Here 0.6 is the resolution in arcsec/pixel and 1 arcsec corresponds to 719 km on the Sun.

As AIA channels use broadband filters, only way to convert the observed count rate (DN counts) to physical units of photon energy is to make some assumptions about the spectral distribution of the incoming light (personal communication with Paul Boerner). For the two wavelengths 211 Å and 193 Å, it is assumed that spectral
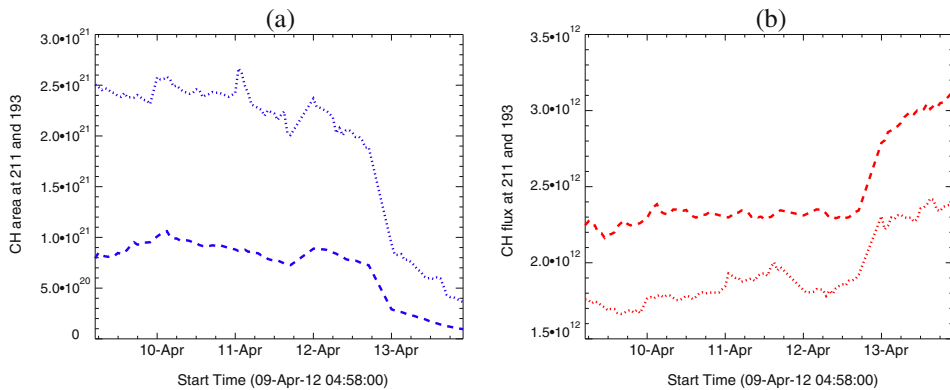

Figure 7. **(a)** Variation of area (cm^2) of the coronal hole in 193 Å (dashed line) and 211 Å (dotted line) pass bands are shown. **(b)** Variation of radiative flux (photons cm^{-2} s^{-1} sr^{-1}) of the coronal hole in 193 Å (dashed line) and 211 Å (dotted line) pass bands occurred on 09-04-2012 with respect to time.

distribution of CH radiation is a delta function. The response function of the filter can be obtained using the sswidl routine aia_get_response.pro that yields CH flux in units of photons $cm^{-2}s^{-1}sr^{-1}$.

As the solar wind has a finite velocity and there is a time delay between the observed wind at 1 AU and the wind emanated from the source (CH) region, we adopt the following method for correction of time delay. If one knows the velocity of solar wind and location of the spacecraft where different wind properties are acquired, with an assumption that solar wind velocity is constant throughout its passage from Sun to the spacecraft, travel time τ from the source region to the region at 1 AU is given as follows

$$\tau = \frac{D}{V_{\text{sw}}}, \tag{2}$$

where D is the distance between source region on the Sun and the spacecraft ($\sim$1 AU) and, V_{sw} is velocity of the solar wind. By knowing the wind velocity V_{sw} at 1 AU, time delay τ is computed by using equation (2) and is compensated for estimation of time of solar wind that probably is originated from the source region (CH).

3. Results

First temporal variation of solar wind velocity data is examined for increase in wind velocity compared to background velocity of $\sim$400 km/s. When a sudden increase in velocity of wind occurs (temporal variation of velocity of wind as illustrated in Figure 2, on 01-06-2013), that time is taken as the starting time of high speed solar wind. By knowing the distance D and by using equation (2) and the observed wind velocity V_{sw} (assuming wind velocity is constant throughout from the source to the place of observation), travel time is computed and is subtracted from the day of observation. For example, in the present study, solar wind velocity jump started at 1st June 2013, 12:30 UT. So computation of travel time yields $\sim$2.6 days. Hence after
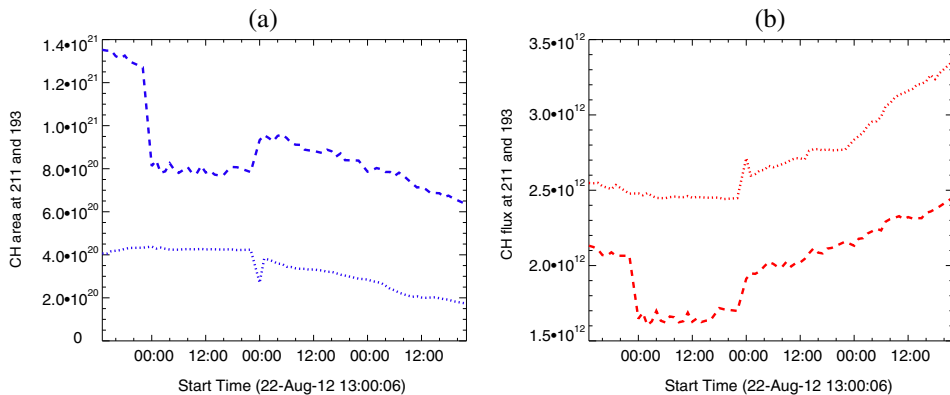

Figure 8. (a) Variation of area (cm^2) of the coronal hole in 193 Å (dashed line) and 211 Å (dotted line) pass bands are shown. (b) Variation of radiative flux (photons $cm^{-2}\,s^{-1}\,sr^{-1}$) of the coronal hole in 193 Å (dashed line) and 211 Å (dotted line) pass bands occurred on 22-08-2012 with respect to time.

364 *M. Hegde et al.*

subtracting 2.6 days from the day of observation of wind velocity, we consider the CH data from 29th May up to 3rd June, when the wind velocity decreases to background velocity of ∼400 km/s. In order to ensure that solar wind is solely due to the coronal hole, following Janardhan *et al.* (2005), we have computed the following two parameters viz., azimuthal angle of magnetic field and oxygen charge state ratio (O^{7+}/O^{6+}). According to Janardhan *et al.* (2005), a low variance in the magnitude of the magnetic field and very small change in the actual direction of the magnetic

Figure 9(a)–(d). Variation of different parameters viz., proton temperature, magnitude of magnetic field, density and speed of solar wind (CH event 09-04-2012) respectively are shown. In Figure 9(d), dashed vertical lines indicate starting and end time of high speed wind.

field indicate that the solar wind flow during that time is stable and unipolar. Also, Liewer *et al.* (2004) showed that wind from solar wind outflows from active region have higher ratios of O^{7+}/O^{6+} compared to coronal hole sources. Typical value of ratio from coronal holes is <0.2. In order to check these evidences, we have calculated the azimuthal direction of the magnetic field in the ecliptic plane from B_x and B_y, the x and y components of the interplanetary magnetic field (IMF) components in GSE coordinates. Figure 3 shows temporal variation of azimuthal angle for the three events with error bars (computed from rms deviations from B_x and B_y).
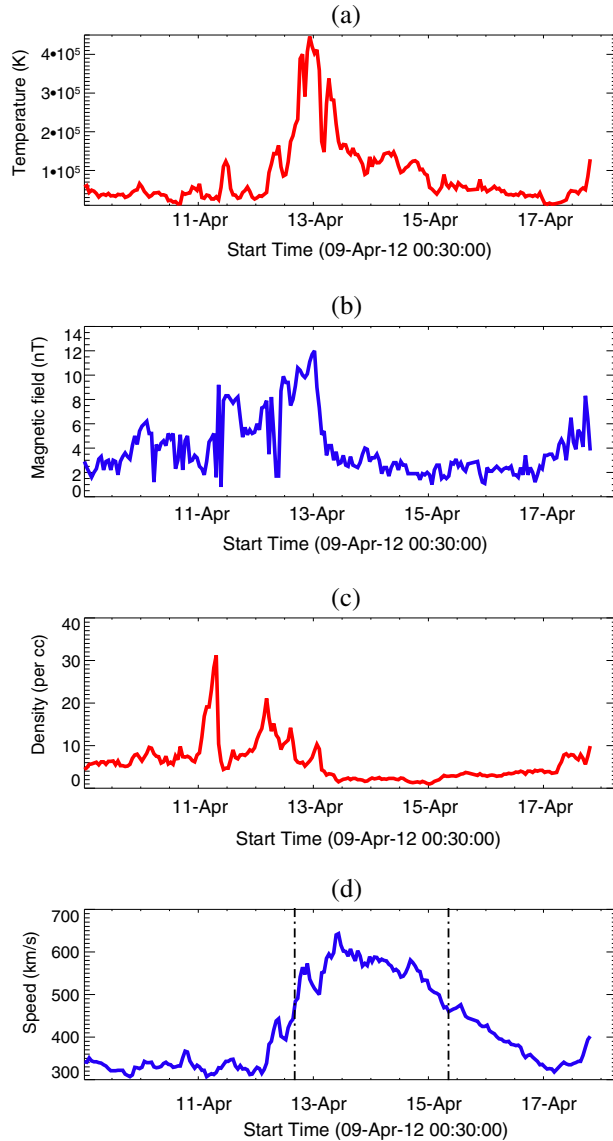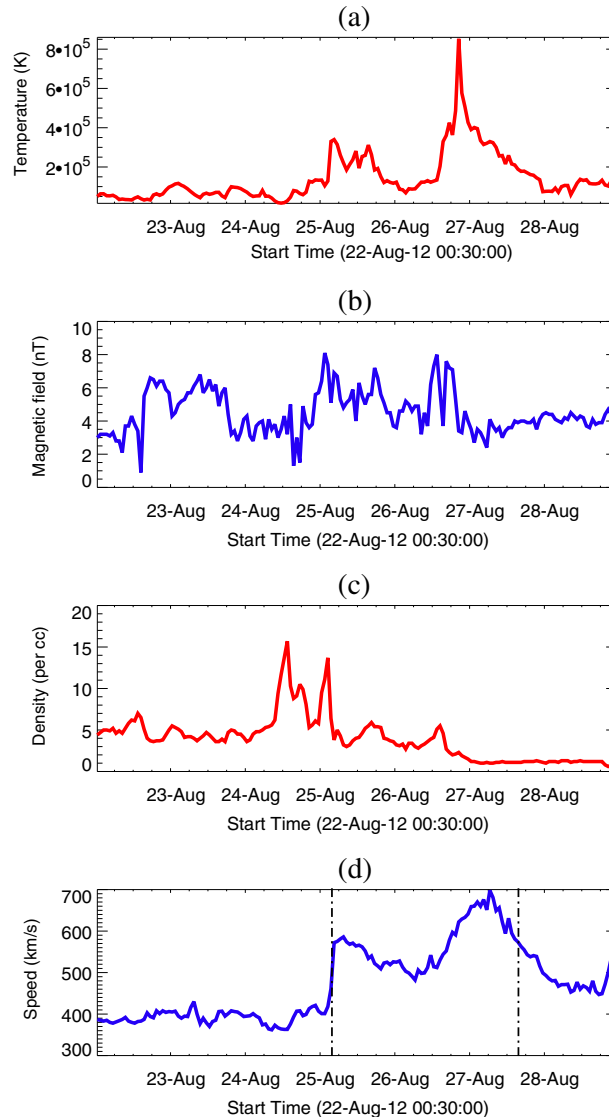

Figure 10(a)–(d). Variation of different parameters viz., proton temperature, magnitude of magnetic field, density and speed of solar wind (CH event 22-08-2012) respectively are shown. In Figure 10(d), dashed vertical lines indicate starting and end time of high speed wind.

The *x*-axis in all the figures indicates Day of the Year (DOY) and *y*-axis represents the magnetic field ($|B|$) and azimuthal angle (Φ). Although, in Figures 3(a) and 3(b), magnitude of the magnetic field varies initially, after certain time the change is negligible. Also, one can notice that in all the three figures azimuthal angle is nearly constant during the period of observation. Figure 4 shows the charge state ratio for the event that occurred in 29 May 2013. Unfortunately, we do not have observed charge state ratio values for the other two events as there was a hardware problem in the ion composition instrument SWICS (private communication with Jason Gilbert). In addition, we have also presented active region maps obtained from the MEES observatory to rule out the influence of active region on the solar wind and confirm that there are no large active regions present during our events as presented in Figure 5. Hence, it is confirmed from all these illustrations (Figures 3–5) that, solar wind is solely due to coronal holes during the observed periods.

After this confirmation, the CH area and radiative flux are computed for each hour. In Figures 6–8, we illustrate temporal variation of CH area and radiative flux for the two wavelength bands. Whereas temporal variation in wind parameters are shown in Figures 2, 9, 10. In order to have a reliable statistics, area and radiative flux values of CH are binned with a step width of 0.5×10^{20} cm^2 in area and 0.2×10^{12} photons cm^{-2} s^{-1} sr^{-1} in the radiative flux respectively. In each binned averages of area and radiative flux of CH, corresponding solar wind parameters are collected. Within

Figure 11(a)–(d). For 193 Å wavelength band, the association of CH area with solar wind parameters are shown. Red continuous line represents a least-square fit of the form $Y = MX + C$ (where Y is the different physical parameter of the solar wind, X is the area of CH, M and C are constants of least square fit) to the observed values. Correlation coefficient and its significance are computed and are overplotted on different plots.

each bin, average, standard deviation σ and error bar $\frac{\sigma}{\sqrt{N}}$ (where N is the number of data points in each bin) are computed. For probing the association between CH and wind parameters, correlation coefficient is computed. Further, both the variables (CH and wind parameters) are subjected to a linear least square fit and the obtained relationship between both the parameters are over plotted in different plots.

For two wavelength channels (193 Å and 211 Å), physical parameters of CH such as area and radiative flux versus solar wind parameters viz., proton density, proton temperature, solar wind velocity and magnitude of magnetic field are presented as scatter plots (Figures 11–14) respectively. One can notice from the results presented in Figures 11–14 that there is a strong positive association between different physical parameters of high speed solar wind with coronal hole area (Figures 11, 12) and a strong negative association with radiative flux (Figures 13, 14) of CH. Latter result is not surprising as area of CH increases radiative flux decreases (see Fig. 12 of Hiremath & Hegde 2013) and hence has an inverse correlative relationship between CH radiative flux and different wind parameters.

Tables 2 and 3 show least square fit analysis for the CH that appeared on 29th May 2013 in 211 Å and 193 Å respectively. Tables 4 and 5 show the least square fit analysis for the CH that appeared on 9th April 2012 in 211 Å and 193 Å respectively. Similarly, Tables 6 and 7 show the least square fit analysis carried out for the CH
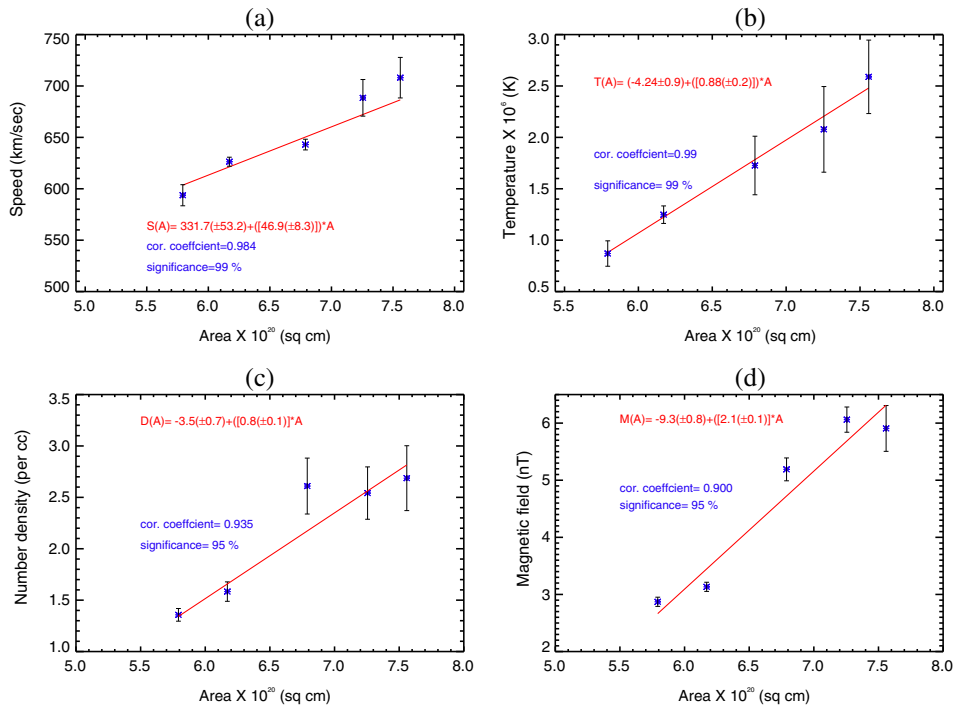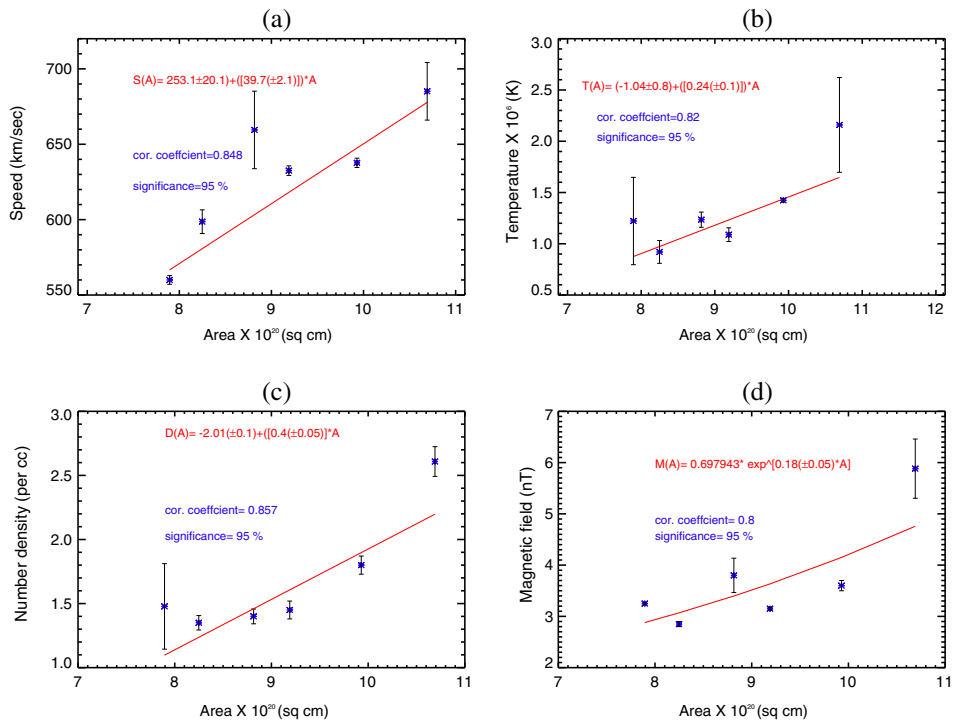

Figure 12(a)–(d). For 211 Å wavelength band, the association of CH area with solar wind parameters are shown. Red continuous line represents a least-square fit of the form $Y = MX + C$ (where Y is the different physical parameters of solar wind, X is the area of CH, M and C are constants of least square fit) to the observed values. Correlation coefficient and its significance are computed and are overplotted on different plots.

Figure 13(a)–(d). For 193 Å wavelength band, the association of CH photon flux (radiative flux) with solar wind parameters are shown. Red continuous line represents a least-square fit of the form $Y = MX + C$ (where Y is the different physical parameters of the solar wind, X is area of CH, M and C are constants of least square fit) to the observed values. Correlation coefficient and its significance are computed and are overplotted on different plots.
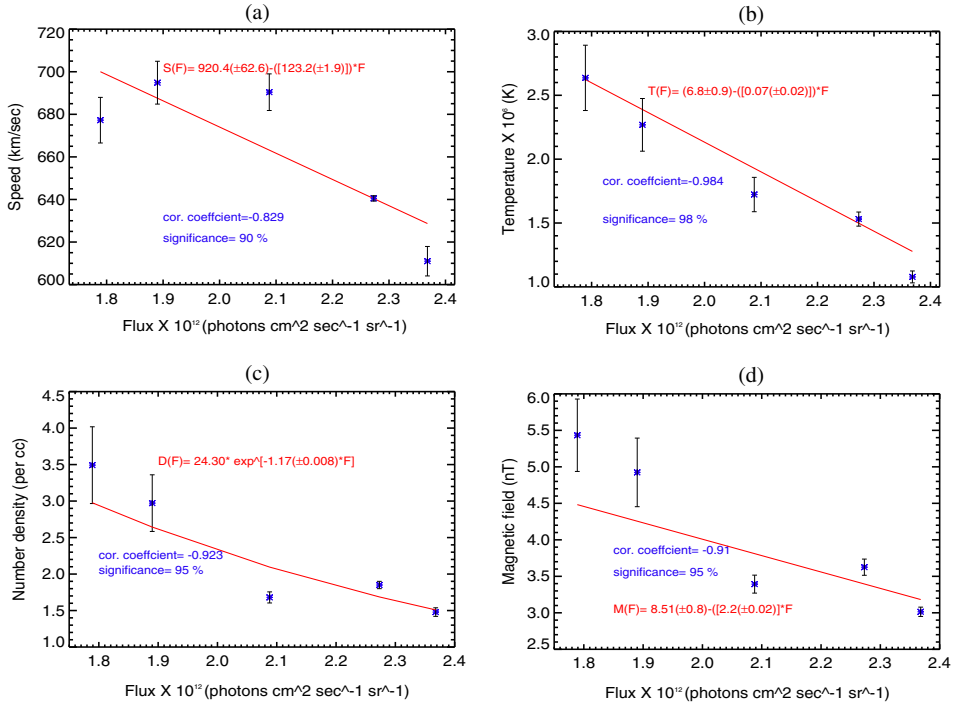
observed on 22nd August 2012 in 211 Å and 193 Å respectively. Tables 8, 9 and 10 show correlation analysis between coronal hole parameters (area and radiative flux) and solar wind parameters. Significance of each correlation coefficient (linear Pearson) is found from the Student t-distribution for all the three events studied.

4. Discussion and conclusions

One can notice from Figure 11 that, for the 193 Å band, 30% increase in CH area is associated with 19% increase in wind speed, 98% increase in density, 111% increase in magnetic field and 197% increase in temperature of solar wind respectively. Whereas in Figure 12, for the 211 Å band, 35% changes in CH area is associated with 22% increase in wind speed, 93% increase in density, 106% increase in magnetic field and 195% increase in temperature of solar wind respectively.

In the same way, in Figure 13, for the 193 Å band, 32% increase of radiative flux is associated with 36% decrease in wind speed, 136% decrease in density, 80% decrease in magnetic field and 144% decrease in temperature of solar wind respectively. Similarly for the 211 Å band, results presented in Fig. 14 suggest 18% increase of radiative flux is associated with 15% decrease in wind speed, 113%

decrease in density, 178% decrease in magnetic field and 171% decrease in temperature of the solar wind respectively. For both the wavelength bands, either percentage increase or decrease of association between CH and wind parameters is nearly the same although both the wavelengths originate at different heights.

It is interesting to know that at 1 AU whether radiative energy probably originated from the CH is same as kinetic or thermal energy density of solar wind. For this purpose, as an example, 29-05-2013 CH event is considered and radiative flux from the observed period is integrated over time to eliminate the s^{-1} factor. Then assumption of the plasma of CH in thermodynamic equilibrium yields radiative energy of $\sim$3.37 $\times 10^6$ ergs cm^{-2} sr^{-1} and $\sim$8.59 $\times 10^5$ ergs cm^{-2} sr^{-1} for 193 Å and 211 Å wavelengths respectively. Then multiplying the energy with steradian, the unit sr^{-1} is removed. To get energy density, the above values are divided by the unit cm that has a dimension of radius of CH (assuming that CH is circular, radius is obtained). For the two wavelengths, the average energy density of observed CH at 1 AU is found to be $\sim$8.4 $\times 10^{-10}$ ergs cm^{-3} for 193 Å and $\sim$0.88 $\times 10^{-10}$ ergs cm^{-3} for 211 Å respectively. However, it is interesting to know whether radiative energy emitted by the CH at two wavelengths is same as total (thermal and kinetic) energy of the solar wind. Solar wind total energy density ($\frac{1}{2}\rho V_{sw}^2 + \frac{1}{2}kT$, where ρ is the density, V_{sw} is the solar wind speed, k is the Boltzmann constant and T is the temperature) turns out
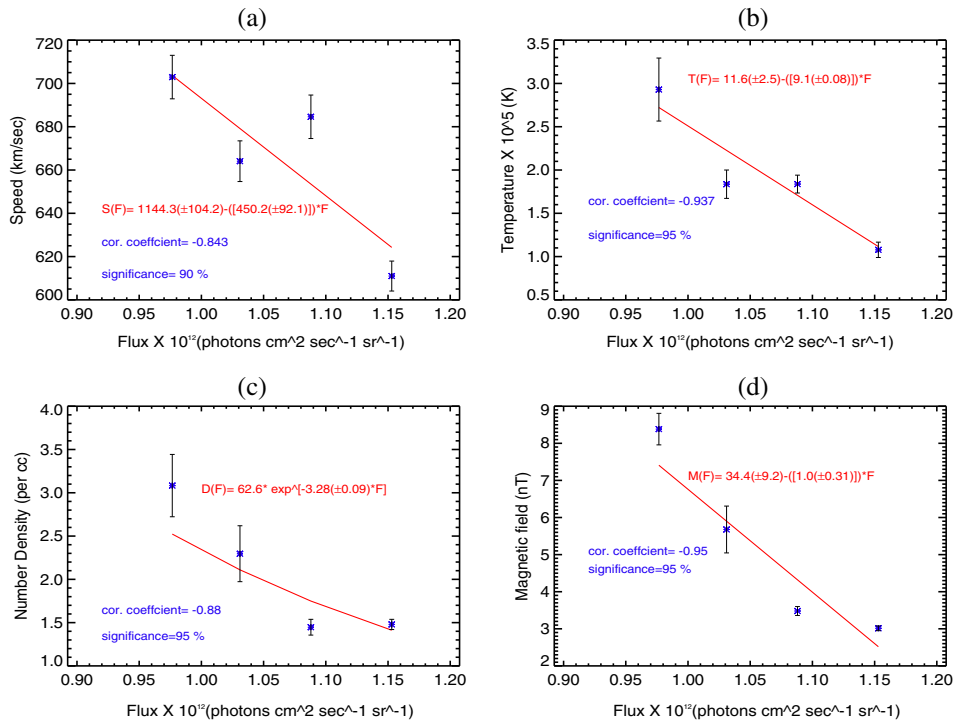
Figure 14(a)–(d). For 211 Å wavelength band, the association of CH photon flux with solar wind parameters are shown. Red continuous line represents a least-square fit of the form $Y = MX + C$ (where Y is the different physical parameters of solar wind, X is the area of CH, M and C are constants of least square fit) to the observed values. Correlation coefficient and its significance are computed and are overplotted on different plots.

Table 2. For the wavelength 211 Å, least-square fits between CH area and radiative flux with different parameters of solar wind observation on 29th May 2013.

Indices	Law	χ^{2***}
V	$(253.1 \pm 20.1) + (39.7 \pm 2.1)A$	0.78
D	$(-2.01 \pm 0.1) + (0.4 \pm 0.05)A$	0.67
T	$(-130233 \pm 732) + (27587 \pm 77)A$	0.87
$|B|$	$(0.69 \pm 0.1) * \exp(0.18 \pm 0.05)A$	0.61
V	$(1144.3 \pm 104.2) - (450.2 \pm 92.1)R$	0.89
D	$(62.6 \pm 3.2) * \exp(-3.28 \pm 0.09)R$	0.57
T	$(1161578 \pm 5894) - (910684 \pm 5282)R$	0.54
$|B|$	$(34.4 \pm 9.2) - (1.0 \pm 0.31)R$	0.98

V is velocity of the solar wind; D is the density of the solar wind; T is the temperature of the solar wind; $|B|$ is the magnitude of the magnetic field of the solar wind; A is the area of the coronal hole; R is the radiative flux of the coronal hole; ***Low value ($\leq$ number of data points considered for the analysis) of χ^2 suggests very good least square and it is not by chance.

Table 3. For the wavelength 193 Å, least-square fits between CH area and radiative flux with different parameters of solar wind observation on 29th May 2013.

Indices	Law	χ^2
V	$(331.7 \pm 53.2) + (46.9 \pm 8.3)A$	0.67
D	$(-3.5 \pm 0.7) + (0.8 \pm 0.1)A$	0.54
T	$(-436346 \pm 1020) + (90539 \pm 159)A$	1.1
$|B|$	$(-9.3 \pm 0.8) + (2.1 \pm 0.1)A$	0.80
V	$(920.4 \pm 62.6) - (123.2 \pm 1.9)R$	0.87
D	$(24.3 \pm 1.2) * \exp(-1.17(\pm 0.008)R$	0.68
T	$(678080 \pm 8860) - (232399(\pm 1424)R$	0.84
$|B|$	$(8.51 \pm 0.8) - (2.2 \pm 0.02)R$	0.74

Table 4. For the wavelength 211 Å, least-square fits between CH area and radiative flux with different parameters of solar wind observation on 9th April 2012.

Indices	Law	χ^2
V	$(322.9 \pm 14.1) + (9.4 \pm 0.8)A$	0.8
D	$(3.99 \pm 0.14) - (0.08 \pm 0.01)A$	0.6
T	$(21872 \pm 3146) + (3059 \pm 461)A$	0.84
$|B|$	$(2.08 \pm 0.11) + (0.05 \pm 0.02)A$	0.56
V	$(817.4 \pm 29.1) - (181.9 \pm 13.5)R$	0.39
D	$(24.88 \pm 4.97) * \exp(-0.88 \pm 0.08)R$	0.58
T	$(2.73 \pm 0.35) - (0.96 \pm 14)R$	0.47
$|B|$	$(12.6 \pm 2.1) - (4.4 \pm 1.2)R$	1.2

to be $\sim 9 \times 10^{-9}$ ergs cm^{-3}. Similar kind of analysis is performed for 09-04-2012 (Figures 9 and 7) and 22-08-2012 events (Figures 10 and 8).

Table 5. For the wavelength 193 Å, least-square fits between CH area and radiative flux with different parameters of solar wind observation on 9th April 2012.

Indices	Law	χ^2
V	$(351.9 \pm 6.6) + (18.4 \pm 1.4)A$	0.73
D	$(2.93 \pm 0.5) * \exp(0.06 \pm 0.01)A$	0.84
T	$(26696.9 \pm 10.1) * \exp(0.22 \pm 0.02)A$	0.69
$|B|$	$(0.51 \pm 0.1) + (0.81 \pm 0.04)A$	0.68
V	$(953.8 \pm 60.3) - (188.4 \pm 20.2)R$	0.59
D	$(18.6 \pm 2.6) * \exp(-0.62 \pm 0.09)R$	0.87
T	$(2.44 \pm 0.36) - (0.67 \pm 11)R$	0.78
$|B|$	$(122.1 \pm 2.4) * \exp(-1.3 \pm 0.08) * R$	0.81

Table 6. For the wavelength 211 Å, least-square fits between CH area and radiative flux with different parameters of solar wind observation on 22nd August 2012.

Indices	Law	χ^2
V	$(427.3 \pm 37.1) + (14.3 \pm 4.1)A$	0.88
D	$(-5.07 \pm 1.1) + (0.9 \pm 0.2)A$	0.26
T	$(-52315.4 \pm 1000.8) + (25125 \pm 899.4)A$	0.49
$|B|$	$(0.45 \pm 0.1) + (0.55 \pm 0.09)A$	0.58
V	$(622.5 \pm 36.1) - (44.9 \pm 9.4)R$	0.98
D	$(10.64 \pm 1.3) - (3.6 \pm 0.06)R$	0.47
T	$(3.03 \pm 0.6) - (0.68 \pm 0.09)R$	0.76
$|B|$	$(11.2 \pm 1.4) - (2.6 \pm 0.08)R$	0.40

Table 7. For the wavelength 193 Å, least-square fits between CH area and radiative flux with different parameters of solar wind observation on 22nd August 2012.

Indices	Law	χ^2
V	$(413.8 \pm 35.1) + (60.5 \pm 3.1)A$	0.75
D	$(0.35 \pm 0.1) * \exp(0.57 \pm 0.02)A$	0.59
T	$(-42271.3 \pm 2045.4) + (93041 \pm 991.4)A$	1.2
$|B|$	$(2.98 \pm 0.37) + (0.60 \pm 0.1)A$	0.83
V	$(1299.5 \pm 74.3) - (266.9 \pm 24.8)R$	0.91
D	$(35.3 \pm 3.1) * \exp(-1.19(\pm 0.08)R$	0.62
T	$(765799 \pm 88.6) * \exp(-4.15(\pm 0.36)R$	0.93
$|B|$	$(19.8 \pm 2.4) * \exp(-0.53 \pm 0.08)R$	0.64

Table 8. Correlation analysis of area and radiative flux of CH with different parameters of the solar wind for the observation on 29th May 2013.

Index	V_{sw} (km/s)		T_p (K)		$|B|$ (nT)		ρ (g/cm^{-3})	
	Cor. coeff.	Signif.	Cor. coeff.	Signif.	Cor. coeff.	Signif.	Cor. coeff.	Signif.
CH area in 211	0.848	95%	0.82	95%	0.80	95%	0.857	95%
CH radiance in 211	−0.843	90%	−0.937	95%	−0.95	95%	−0.88	95%
CH area in 193	0.984	99%	0.98	99%	0.90	95%	0.935	95%
CH radiance in 193	−0.829	90%	−0.984	90%	−0.91	95%	−0.923	95%

V_{sw} is velocity of the solar wind, T_p is proton temperature of the solar wind, $|B|$ is the magnitude of the magnetic field of the solar wind, ρ is the density of the solar wind, Cor. coeff. is the correlation coefficient, Signif. is significance of correlation coefficient computed from student-t distribution.

Table 9. Correlation analysis of area and radiative flux of CH with different parameters of the solar wind for the observation on 9th April 2012.

Index	V_{sw} (km/s)		T_p (K)		$|B|$ (nT)		ρ (g/cm^{-3})	
	Cor. coeff.	Signif.	Cor. coeff.	Signif.	Cor. coeff.	Signif.	Cor. coeff.	Signif.
CH area in 211	0.989	99%	0.83	95%	0.77	95%	0.66	90%
CH radiance in 211	−0.64	90%	−0.89	95%	−0.85	95%	−0.86	95%
CH area in 193	0.974	98%	0.926	98%	0.91	95%	0.70	90%
CH radiance in 193	−0.700	90%	−0.987	98%	−0.700	90%	−0.700	90%

Table 10. Correlation analysis of area and radiative flux of CH with different parameters of solar wind for the observation on 22nd August 2012.

Index	V_{sw} (km/s)		T_p (K)		$|B|$ (nT)		ρ (g/cm^{-3})	
	Cor. coeff.	Signif.	Cor. coeff.	Signif.	Cor. coeff.	Signif.	Cor. coeff.	Signif.
CH area in 211	0.985	98%	0.80	95%	0.989	99%	0.81	95%
CH radiance in 211	−0.64	90%	−0.54	90%	−0.83	95%	−0.94	95%
CH area in 193	0.90	95%	0.60	90%	0.90	95%	0.90	95%
CH radiance in 193	−0.976	98%	−0.900	95%	−0.60	90%	−0.700	90%

Although we have similar order of CH radiative and solar wind energy at 1 AU, the mechanism as to how the CH radiative energy is converted into solar wind energy is beyond the scope of this study. In all the three CHs considered in this study, both the magnitude of energy at 193 Å wavelength and the solar wind energy at 1 AU nearly match giving a clue that solar wind might have originated close to the height of line formation of 193 Å. Large number of observed data of CH taken at different wavelengths can shed more light on the association between CH and the solar wind parameters and, further confirmation that solar wind is originated around the same height of origin of 193 Å is to be verified.

To conclude this study, using high temporal and spatial SDO/AIA data, coronal hole area and radiative flux are computed. These parameters of coronal hole are investigated for association with the solar wind parameters like velocity, temperature, magnetic field and particle number density. It is found that there exists a positive correlation between coronal hole area and an inverse correlation of radiative flux with different solar wind parameters. Also, coronal hole radiative energy computed at 1 AU is almost same as solar wind energy at 1 AU suggesting that solar wind is solely originated due to the near-equatorial coronal hole and most likely is originated around the same height where 193 Å line is formed in the corona.

References

Abramenko, V., Yurchyshyn, V., Watanabe, H. 2009, *Sol. Phys.*, **260**, 43–57.

Akiyama, S., Gopalswamy, N., Yashiro, S., Mäkelä, P. 2013, *PASJ*, **65**, 15.

Altschuler, M. D., Trotter, D. E., Orrall, F. Q. 1972, *Sol. Phys.*, **26**, 354–365.

Axford, W. I., McKenzie, J. F. 1997, in: *The Solar Wind*, edited by J. R. Jokipii, C. P. Sonett and M. S. Giampapa, Cosmic Winds and the Heliosphere, p. 31.

Biermann, L. 1951, *ZAp*, **29**, 274.

Bromage, B. J. I., Browning, P. K., Clegg, J. R. 2001, *Space Sci. Rev.*, **97**, 13–16.

de Toma, G. 2011, *Sol. Phys.*, **274**, 195–217.

Gosling, J. T., Pizzo, V. J. 1999, *Space Sci. Rev.*, **89**, 21–52.

Hiremath, K. M., Hegde, M. 2013, *ApJ*, **763**, 137.

Janardhan, P., Fujiki, K., Kojima, M., Tokumaru, M., Hakamada, K. 2005, *J. Geophys. Res. (Space Phys.)*, **110**, 8101.

Janardhan, P., Fujiki, K., Sawant, H. S., Kojima, M., Hakamada, K., Krishnan, R. 2008a, *J. Geophys. Res. (Space Phys.)*, **113**, 3102.

Janardhan, P., Tripathi, D., Mason, H. E. 2008b, *A&A*, **488**, L1–L4.

Kahler, S. W., Hudson, H. S. 2001, *J. Geophys. Res.*, **106**, 29239–29248.

Krieger, A. S., Timothy, A. F., Roelof, E. C. 1973, *Sol. Phys.*, **29**, 505–525.

Krista, L. D. 2012, *The Evolution and Space Weather Effects of Solar Coronal Holes*, Ph.D. thesis, University of Dublin.

Lemen, J. R. *et al.* 2012, *Sol. Phys.*, **275**, 17–40.

Liewer, P. C., Neugebauer, M., Zurbuchen, T. 2004, *Sol. Phys.*, **223**, 209–229.

Madjarska, M. S., Wiegelmann, T. 2009, *A&A*, **503**, 991–997.

Marsch, E. 1999, *Space Sci. Rev.*, **87**, 1–24.

McComas, D. J., Elliott, H. A., von Steiger, R. 2002, *Geophys. Res. Lett.*, **29**, 1314.

Nolte, J. T., Krieger, A. S., Timothy, A. F., Gold, R. E., Roelof, E. C., Vaiana, G., Lazarus, A. J., Sullivan, J. D., McIntosh, P. S. 1976, *Sol. Phys.*, **46**, 303–322.

Obridko, V. N., Shelting, B. D. 2011, *Sol. Phys.*, **270**, 297–310.

Obridko, V. N., Shelting, B. D., Livshits, I. M., Asgarov, A. B. 2009, *Sol. Phys.*, **260**, 191–206.

Parker, E. N. 1958, *ApJ*, **128**, 677.

Robbins, S., Henney, C. J., Harvey, J. W. 2006, *Sol. Phys.*, **233**, 265–276.

Rotter, T., Veronig, A. M., Temmer, M., Vršnak, B. 2012, *Sol. Phys.*, **281**, 793–813.

Sakao, T., Kano, R., Narukage, N., Kotoku, J., Bando, T., DeLuca, E. E., Lundquist, L. L., Tsuneta, S., Harra, L. K., Katsukawa, Y., Kubo, M., Hara, H., Matsuzaki, K., Shimojo, M., Bookbinder, J. A., Golub, L., Korreck, K. E., Su, Y., Shibasaki, K., Shimizu, T., Nakatani, I. 2007, *Science*, **318**, 1585.

Shashanka, R.G., Hiremath, K. M., Ramsubramanian, V. 2014a, *On the relationship between masses of Sun like G-stars and their exoplanets*, **1**, 99.

Shashanka, R. G., Hiremath, K. M., Ramsubramanian, V., Hegde, M. 2014b, *Mass relationship between sun like stars and their exoplanets*, submitted to *MNRAS*.

Sheeley, N. R., Harvey, J. W. 1981, *Sol. Phys.*, **70**, 237–249.

Shugai, Y. S., Veselovsky, I. S., Trichtchenko, L. D. 2009, *Geomagnetism and Aeronomy*, **49**, 415–424.

Subramanian, S., Madjarska, M. S., Doyle, J. G. 2010, *A&A*, **516**, A50.

Tlatov, A., Tavastsherna, K., Vasil'eva, V. 2014, *Sol. Phys.*, **289**, 1349–1358.

Verbanac, G., Vršnak, B., Veronig, A., Temmer, M. 2011, *A&A*, **526**, A20.

Vršnak, B., Temmer, M., Veronig, A. M. 2007a, *Sol. Phys.*, **240**, 315–330.

Vršnak, B., Temmer, M., Veronig, A. M. 2007b, *Sol. Phys.*, **240**, 331–346.

Wang, Y.-M., Sheeley, N. R. 1990, *ApJ*, **365**, 372–386.

Wood, B. E. 2006, *Space Sci. Rev.*, **126**, 3–14.

Xia, L. D. 2003, *Equatorial Coronal Holes and Their Relation to the High-Speed Solar Wind Streams*, Ph.D. thesis, University of Göttingen.

Zhang, J., Woch, J., Solanki, S. K., von Steiger, R. 2002, *Geophys. Res. Lett.*, **29**, 1236.
Zhang, J., Woch, J., Solanki, S. K., von Steiger, R., Forsyth, R. 2003, *J. Geophys. Res. (Space Phys.)*, **108**, 1144.
Zirker, J. B. 1977, *Coronal holes and high speed wind streams: a monograph from Skylab solar workshop I.*